# PCCP

Accepted Manuscript

ROYAL SOCIETY OF CHEMISTRY

www.rsc.org/pccp

# Revealing the role of $Pb^{2+}$ in the stability of organic-inorganic hybrid perovskite $CH_3NH_3Pb_{1-x}Cd_xI_3$. An experimental and theoretical study

Javier Navas,*[,a] Antonio Sánchez-Coronilla,*[,b] Juan Jesús Gallardo,[a] Elisa I. Martín,[c] Norge C. Hernández,[d] Rodrigo Alcántara,[a] Concha Fernández-Lorenzo,[a] Joaquín Martín-Calleja[a]

[a]Departamento de Química Física, Facultad de Ciencias, Universidad de Cádiz, E-11510 Puerto Real (Cádiz), Spain; [b]Departamento de Química Física, Facultad de Farmacia, Universidad de Sevilla, E-41012 Sevilla, Spain; [c]Departamento de Ingeniería Química, Facultad de Química, Universidad de Sevilla, E-41012 Sevilla, Spain; and [d]Departamento de Física Aplicada I, Escuela Técnica Superior de Ingeniería Informática, av. Reina Mercedes, Universidad de Sevilla, E-41012 Sevilla, Spain.

Corresponding Authors:

* Javier Navas (javier.navas@uca.es); Antonio Sánchez-Coronilla (antsancor@us.es).

## Table of Contents entry

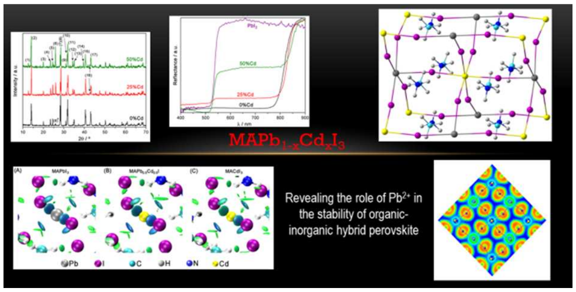

Experimental and theoretical analysis revealing the role of $Pb^{2+}$ in the stability of organic-inorganic hybrid perovskites

# Abstract

This paper presents the synthesis of organic-inorganic hybrid perovskite $CH_3NH_3Pb_{1-x}Cd_xI_3$. The effect of incorporating $Cd^{2+}$ or $Pb^{2+}$ on the stability of the perovskite structure was analysed from a theoretical and experimental viewpoint. The XRD results showed that the tetragonal perovskite structure was formed for values of x of up to 0.5, which seems to indicate that the presence of a considerable amount of $Pb^{2+}$ is necessary to stabilise the structure. In turn, UV-Vis spectroscopy showed how the presence of $Cd^{2+}$ led to a reduction in the optical band gap of the perovskite structure of up to 9% for $CH_3NH_3Pb_{0.5}Cd_{0.5}I_3$ with regards to the $MAPbI_3$ structure. Moreover, periodic-DFT calculations were performed to understand the effect of the increased concentration of Cd on the structural and electronic properties of $MAPbI_3$ perovskites. The analysis of both the ELF and the non-covalent interaction (NCI) index show the important role played by the $Pb^{2+}$ ions in stabilizing this kind of hybrid perovskite structures. Finally, the DOS analysis confirmed the experimental results obtained using UV-Vis spectroscopy. The theoretical band gap values decreased as the concentration of Cd increased.

## 1. Introduction

Perovskites have many fascinating properties, including superconductivity, ferroelectricity, high thermoelectric power or optical properties.[1] Thanks to these properties, perovskites have been used as sensors, catalysts and optoelectronic material.[2-4] Nowadays, organic-inorganic perovskites based on halides are studied because they perform well in photovoltaic applications.[5-7] Perovskites have a specific crystal structure with the $ABX_3$ formula. The crystal structure of the $ABX_3$ compounds consist of a three-dimensional lattice of corner sharing $BX_6$ octahedra, where B is a bivalent metal cation, A is a monovalent organic cation that is small enough to fit into the structure, and X is a halogen.[8] A methyl ammonium cation ($[CH_3NH_3]^+$, MA) is the most usual monovalent organic cation in several applications. Moreover, interesting examples of this kind of perovskites are $CH_3NH_3BX_3$, where B = $Sn^{2+}$, $Pb^{2+}$; X = $Cl^-$, $Br^-$, $I^-$. In turn, methyl ammonium lead iodide ($MAPbI_3$) has brought about a revolution in photovoltaic applications thanks to its high efficiency, which reaches 18%.[7] Thus, the crystalline structure and good photonic absorption are two vital factors in the high performance of this kind of compound in solar cells. The substitution of some elements in $MAPbI_3$ can make it possible to control the optical and electronic properties of perovskites, which can affect the performance of the devices. For example, the substitution of $I^-$ with $Cl^-$ or $Br^-$ has been widely studied; and doping with inorganic cations such as $Sn^{2+}$, $Sr^{2+}$, or $Ca^{2+}$ in $Pb^{2+}$ sites has been analysed to understand its effect on optical and electronic properties.[5, 9-12]

Thus, this article studies the effect on the structural stability and electronic properties of the introduction of $Pb^{2+}$ or $Cd^{2+}$ ions in position B of an $ABX_3$-type perovskite, where A = MA and X = $I^-$. To do this, synthesized samples were characterised using elemental analysis techniques such as the CHNS technique or X-ray fluorescence (XRF) to corroborate the amount of $Pb^{2+}$ and $Cd^{2+}$ introduced; X-ray diffraction (XRD) determined the crystalline phases present in the samples; X-ray photon spectroscopy (XPS) determined the chemical bonding states; and UV-Vis spectroscopy in the diffuse reflectance mode (DR-UV-Vis) was used to establish the optical band gap of the samples. In addition, from a theoretical perspective, periodic density functional theory (DFT-periodic) calculations were performed to rationalize the experimental information on this topic. Therefore, to explore the electronic and structural effects of increasing the concentration of Cd, the structures $(MA)_4Pb_4I_{12}$, $(MA)_4Pb_3CdI_{12}$, $(MA)_4Pb_2Cd_2I_{12}$ $(MA)_4Pb_1Cd_3I_{12}$ and $(MA)_4Cd_4I_{12}$ were optimised. The analysis of both the electron localization function (ELF)[13-17] and the non-covalent interaction (NCI)[18] shed light on the bonding interactions established within these hybrid systems, highlighting the important role of the $Pb^{2+}$ ions in the stabilization of this kind of hybrid structures. The density of State (DOS) and band structure results taking into account the spin-orbit coupling (SOC) effects were in agreement with the tendency forecast experimentally, showing a decrease in the optical band gap energy as the concentration of $Cd^{2+}$ increased.

## 2. Experimental and Computational section

### 2.1. Experimental

#### 2.1.1. Reagents

All the reagents were from commercial sources and used without further purification. The hydroidic acid (HI, 57 wt% in water) was from Aldrich; the methylamine ($CH_3NH_2$, 33 wt% in ethanol), diethyl ether ($Et_2O$, purity ≥ 99.8%), led iodide ($PbI_2$, purity 99%), cadmium iodide ($CdI_2$, purity 99.999%), and γ-butyrolactone (purity ≥ 99%) were from Sigma-Aldrich.

### 2.1.2. Synthesis

The synthesis of the perovskite phases was performed by means of the reaction of $CH_3NH_3I$ and the nominal quantities of $PbI_2$ and $CdI_2$. First, the $CH_3NH_3I$ was synthesized following the procedure:[12, 19, 20] HI (10 mL, 0.076 mol) and $CH_3NH_2$ (11.33 mL, 0.091 mol) were stirred in an ice bath for 2 h. Next, the mixture was evaporated at 50 ºC for 1 h, and $CH_3NH_3I$ was obtained. Then, the solid was cleaned three times using $Et_2O$.

For the synthesis of the perovskite phase, a mixture was prepared of $CH_3NH_3I$ (0.395 g) and the corresponding stoichiometric amount to obtain nominal concentrations of Cd (Cd/(Cd+Pb)) of 0, 25, 50, 75 y 100 at.% in γ-butyrolactone (2 mL) at 60 ºC for 18 h.

### 2.1.2. Characterization

The elemental analysis was performed using two instrumental techniques. The CHNS technique was used to obtain the amount of C, H and N, using an elemental analyser supplied by Leco®, model CHNS932. Also, X-ray fluorescence (XRF) was performed to determine the amount of Pb, Cd and I using a sequential XRF spectrometer supplied by Bruker®, model Pioneer S4. X-ray Diffraction (XRD) was used to determine the crystalline phases in the samples. The patterns were recorded using a diffractometer supplied by Bruker®, model D8 Discover, with Cu-Kα radiation. The scan conditions were from 10 to 70º in 2θ with a resolution of 0.02º, 40 kV and 40 mA. The optical band gap ($E_g$) values were determined from diffuse reflectance UV-Vis (DR-UV-Vis) measurements. The spectra were collected by using a system assembled in our laboratory composed of an integrating sphere supplied by Spectra Tech®, a USB2000+ spectrometer supplied by Ocean Optics®, and a Xe lamp, model ASB-XE-175, supplied by Spectral Products®, as the illumination source. Moreover, X-ray photoelectron spectroscopy (XPS) was used to study the chemical bonding states and the chemical compositions of the samples. The spectra were obtained using a Kratos® Axis UltraDLD spectrometer, with monochromated Al-Kα radiation (1486.6 eV) and 20 eV pass energy. The binding energy was given with an accuracy of 0.01 eV. Electrostatic charging effects were stabilised with the help of a specific device developed by Kratos®.

### 2.2. Computational framework

DFT-periodic calculations were performed using the Vienna Ab Initio Simulation Package (VASP)[21-24] with the projector-augmented wave (PAW) method.[25, 26] The number of plane waves in VASP was controlled by a cut-off energy, chosen according to the pseudopotential and set in our calculations to $E_{\mathrm{cut}}$=500 eV to satisfactorily describe the system.[12] In this way, the value of the cut-off was chosen by increasing around 30% the highest value defined for all pseudopotentials used, i.e. carbon and nitrogen. The electron exchange and correlation were treated within the generalised gradient approximation (GGA).[27] In the case of GGA, Perdew-Burke-Ernzerhof (PBE)[27] functionals were used that provide geometrical structures and relative stabilities for hybrid perovskites in good agreement with experimental data, as reported elsewhere.[11, 28-30] Both the cell shape and atomic positions were optimised using a conjugate-gradient algorithm, where the iterative relaxation of atomic positions was stopped when the forces on the atoms were less than 0.01 eV/Å. Also, a Gaussian smearing with $k_BT$=0.1365 eV was applied.

Perovskite tetragonal phase was characterised by the I4/mcm space group.[30] The tag KSPACING determined the number of k-points in the mesh. A value of 0.4 for sampling the Brillouin zone for perovskite bulk was enough to obtain negligible changes in the optimised cell parameters and energy. The resulting cell parameters were *a* = 8.912 Å, *c* = 12.707 Å for the tetragonal phase, in agreement with the experimental values (*a* = 8.874 Å, *c* = 12.671 Å).[30]

The $(MA)_4Pb_4I_{12}$ cell was optimised as a model for the tetragonal phase of perovskite. The incorporation of each proportion of Cd into the structure was performed in substitutional positions. The Cd atom substitutes the Pb atom in the perovskite structure taking into account the equivalent sites. The structures $(MA)_4Pb_3CdI_{12}$, $(MA)_4Pb_2Cd_2I_{12}$ $(MA)_4Pb_1Cd_3I_{12}$ and $(MA)_4Cd_4I_{12}$ were optimised. The selected structures were adequate to represent qualitatively the experimental concentrations within DFT with a periodic boundary condition framework. It is well known the structural disorder associated to the MA rotation in this kind of hybrid perovskites.[5, 30, 31] In a previous work we tested different orientations of MA within the tetragonal structure, reporting the most stable configuration for each doped structure.[12] This structure has been used as origin for optimizing the structures used in this work.

The density of states (DOS) and projected density of states (PDOS) for the relaxed structures were obtained using the tetrahedron method with Blöchl corrections[32] and a KSPACING of 0.3. For all the systems, DFT+U[33] calculations were performed to take into account the on-site Coulomb interaction. A U value of 5 eV was used for d orbitals.[34]

Recent works have confirmed a relevant SOC in $MAPbI_3$ due to the strong SOC on Pb atoms leading to a strong band-gap reduction by inducing a large splitting of the conduction levels while the valence band levels are nearly unaffected.[35, 36] Although more computationally demanding, the inclusion of many body perturbation theory, within the GW approach[37, 38] and SOC lead to a good correlation between the band gap values calculated and the experimental ones,[11, 35] because of GW corrections are large and in opposite direction to SOC effect.[35] Nonetheless, a computationally viable alternative that has been recently applied consists of SOC-U which is followed in this work.[39] For $MAPbI_3$ the U value of 9 eV was used for Pb p-orbitals.

Electron localization function (ELF)[13-17] images and structure images were obtained using the Vaspview software[40] and ChemCraft 1.6,[41] respectively. The non-covalent interaction analysis was performed with CRITIC2 software.[42, 43] NCI images were made with VMD software.[44] VMD was developed with NIH support by the Theoretical and Computational Biophysics group at the Beckman Institute, University of Illinois at Urbana-Champaign.

## 3. Results and Discussion

### 3.1. Elemental analysis

The elemental analysis of the samples synthesized (see experimental section) was performed using X-ray fluorescence to determine the amount of $I^-$, $Pb^{2+}$ and $Cd^{2+}$ in the samples. The CHNS technique was used to determine the amount of C, H and N. From the elemental analysis, the weight percent of the elements present in the samples was obtained, and these are shown in Table 1. The percentages of C, H and N are shown together, but are detailed by element in Table S1 in the Electronic Supplementary Information (ESI). In turn, Table 1 shows the atomic/molar proportion of Cd was determined, obtained as the ratio of Cd/(Cd+Pb). It shows that the expected proportions were obtained with only small deviations with respect to the nominal composition.

**Table 1.** Results in weight percentage (wt.%) obtained from the elemental analysis performed using the CHNS and XRF techniques.

| Nominal at% Cd | wt% CHN | wt% I | wt% Pb | wt% Cd | Cd/(Cd+Pb) |
|---|---|---|---|---|---|
| 0.0 | 5.19 | 61.25 | 33.56 | -- | 0.00 |
| 25.0 | 5.39 | 63.71 | 25.98 | 4.92 | 0.26 |
| 50.0 | 5.57 | 66.53 | 17.92 | 9.98 | 0.51 |
| 75.0 | 5.85 | 69.08 | 10.05 | 15.02 | 0.73 |
| 100.0 | 6.11 | 72.14 | -- | 21.75 | 1.01 |

### 3.2. X-Ray Diffraction

Figure 1A shows the XRD patterns for the samples with a nominal atomic Cd proportion of 0 at.%, 25 at.% and 50 at.%, while Figure 1B shows the patterns for the samples with 75 at.% and 100 at.%. The patterns of the samples without Cd show several diffraction peaks, which can be indexed to planes of the tetragonal *I4*/*mcm* space group, as reported previously for $MAPbI_3$ perovskite.[6, 30, 45-47] The assignation of the peaks found in the patterns is shown in Table 2. The peak highlighted as (4) is assigned to the reflection of the plane (211) of the perovskite tetragonal phase, and this reflection is the main difference between the patterns for perovskite tetragonal phase and perovskite cubic phase (*Pm3m* space group). This reflection is inconsistent with cubic symmetry, so the presence of perovskite cubic phase is negligible in our samples.[30] In turn, for the samples without Cd, some peaks (pointed out as (6)*, (12), (14)) are assigned to the residual $PbI_2$ used as a reagent in the synthesis, according to PDF 00-007-0235 reference.

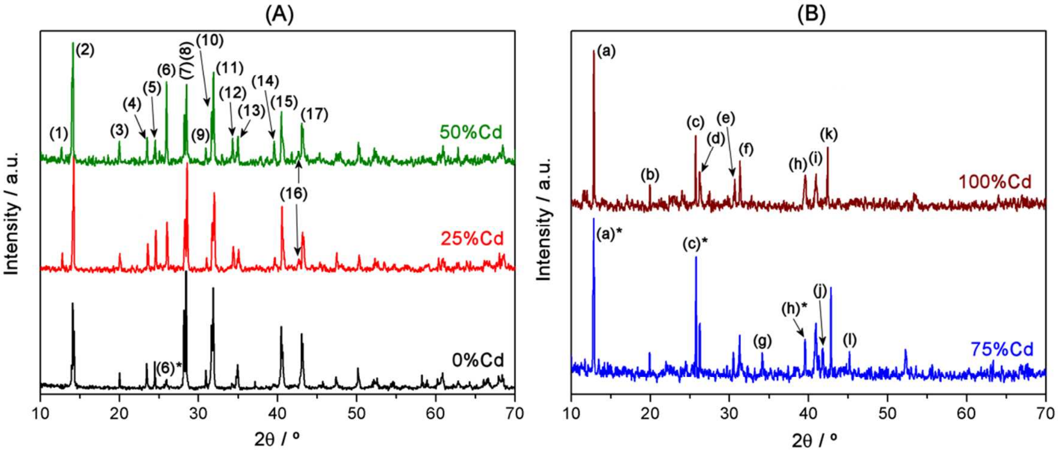

**Figure 1.** XRD patterns of the samples synthesized.

**Table 2.** Assignation of the XRD peaks. Te: Tetragonal perovskite phase; MAI: $CH_3NH_3I$.

| Figure 1A | | | | Figure 1B | | | |
|---|---|---|---|---|---|---|---|
| **Peak** | **Assignation** | **Peak** | **Assignation** | **Peak** | **Assignation** | **Peak** | **Assignation** |
| (1) | $CdI_2$(002)<br>$PbI_2$(001)<br>MAI[a] | (9) | Te(213) | (a) | $CdI_2$(002)<br>MAI[a] | (g) | $PbI_2$(102) |
| (2) | Te(110)(002) | (10) | Te(114)<br>Residual $CdI_2$(103) | (a)* | $CdI_2$(002)<br>$PbI_2$(001)<br>MAI[a] | (h) | $CdI_2$(006) |
| (3) | Te(112)<br>MAI[a] | (11) | Te(222)(310)<br>MAI[a] | (b) | MAI[a] | (h)* | $CdI_2$(006)<br>$PbI_2$(110) |
| (4) | Te(211) | (12) | $PbI_2$(102) | (c) | $CdI_2$(004)<br>MAI[a] | (i) | MAI[a] |
| (5) | Te(200) | (13) | Te[a] | (c)* | $CdI_2$(004)<br>$PbI_2$(002)<br>MAI[a] | (j) | $PbI_2$(111) |
| (6) | $CdI_2$(004)<br>$PbI_2$(002)<br>MAI[a] | (14) | $CdI_2$(006)<br>$PbI_2$(110) | (d) | MAI[a] | (k) | $CdI_2$(110) |
| (6)* | $PbI_2$(002) | (15) | Te[a]<br>Residual $CdI_2$(105)<br>Residual MAI[a] | (e) | MAI[a] | (l) | $PbI_2$(103) |
| (7) | Te(004) | (16) | $CdI_2$(110) | (f) | $CdI_2$(103)<br>MAI[a] | | |
| (8) | Te(220) | (17) | Te(330) | | | | |

[a] Planes not assigned in the references.

Moreover, the XRD patterns obtained for the samples with a nominal Cd composition of 25 at.% and 50 at.% show the peaks assigned to perovskite tetragonal phase (see Table 2). Moreover, the XRD patterns of these samples show peaks (marked as (1), (3), (6), (12), (14), (16)) that can be assigned to $PbI_2$, $CdI_2$ and MAI, used as reagents in the synthesis, according to PDF 00-007-0235, PDF 00-033-0239, PDF 00-030-1797 references, respectively. Moreover, the proportion of the reagents increased with the nominal percentage of Cd, as is clearly observed in the peak pointed out as (6). Therefore, these samples are composed of a mixture of phases. These are tetragonal perovskite phase (*I4/mcm* space group), hexagonal $CdI_2$ (*P63mc* space group), hexagonal $PbI_2$ (*P-3m1* space group) and hexagonal MAI.

Figure 1B shows the patterns for the samples with a nominal Cd percentage of 75 at.% and 100 at.%. The assignation of the peaks is shown in Table 2. The presence of any perovskite phase is not observed in these patterns. Moreover, only the peaks of the reagents are found.

The formability of perovskite structure is estimated based on a geometric factor, known as Goldschmidt's tolerance factor ($t$). For $ABX_3$ perovskites, this factor is described as

$$t = (r_A + r_X)/2^{1/2}(r_B + r_X) \quad (1)$$

where $r_A$, $r_B$ and $r_X$ are the effective ionic radii for A, B and X ions,[48] which in our case are $[CH_3NH_3]^+$, $Pb^{2+}$ or $Cd^{2+}$ and $I^-$, respectively. Goldschmidt's factor is widely accepted as a criterion for the formation of the perovskite structure. Generally, the formation of perovskite structures is generated in the range 0.75-1.00, and an ideal cubic perovskite is expected when $t = 1$, while octahedral distortions are expected for $t < 1$.[49] But, Goldschmidt's tolerance factor does not seem to be sufficient to predict the formation of the perovskite structure, another factor being needed. Li et al. reported the use of the 'octahedral factor' ($\mu$),[49, 50] defined as

$$\mu = {}^{r_B}/_{r_X} \quad (2)$$

According to the literature, for halide perovskites, most perovskites show tolerance factors in the range of 0.813-1.107, and the octahedral factor is higher than 0.442.[49] Thus, we analysed the $MAPbI_3$ and $MACdI_3$ systems. The values for the effective ionic radii of $Pb^{2+}$, $Cd^{2+}$ and $I^-$ were taken from the literature,[51] while the effective ionic radius value of MA ($r_{MA}$) was calculated according to a rigid sphere model with free rotation of its centre of mass. First, the centre of mass of the molecule is detected, and the distances between the centre of mass and all the atoms are estimated. The effective radius of MA is calculated as the sum of the largest distance between centre of mass and an atom, including hydrogen atoms ($r_{CM}$), and the corresponding covalent radius of this atom ($r_{covH}$), which is hydrogen. So, $r_{MA} = r_{CM} + r_{covH}$, where in our case $r_{CM} = 1.51$Å, and according to the literature $r_{covH} = 0.23$Å.[52] Thus, $r_{MA}$ is estimated as 1.74Å, in good agreement with the values found in the literature.[7] The values for the effective ionic radii used and the results for Goldschmidt tolerance factor and octahedral factor for both systems are shown in Table 3. These results show that the $MAPbI_3$ system fulfils both conditions and that $t < 0.9$, which is coherent with obtaining tetragonal perovskite phase in the sample. In turn, the tolerance factor value for the $MACdI_3$ system is within the range established for the formation of perovskite phase, but the octahedral factor value is below the usual limit. This is coherent with perovskite phase not being formed when the proportion of $Cd^{2+}$ in the samples increased.

Thus, from the XRD patterns, it is possible to conclude that an increase in the proportion of $Cd^{2+}$ in the synthesis impedes the formation of perovskite phase. These results are coherent with the UV-Vis spectroscopy results, as shown below.

**Table 3.** Values of the ionic radii used, and the values calculated for Goldschmidt's tolerance factor and 'octahedral factor' for the $MAPbI_3$ and $MACdI_3$ systems.

| Ion | $r$ / Å | Perovskite | $t$ | $\mu$ |
|---|---|---|---|---|
| $[CH_3NH_3]^+$ | 1.74 | $MAPbI_3$ | 0.822 | 0.541 |
| $Pb^{2+}$ | 1.19 | $MACdI_3$ | 0.884 | 0.432 |
| $Cd^{2+}$ | 0.95 | | | |
| $I^-$ | 2.20 | | | |

### 3.3. UV-Vis Spectroscopy

The optical band gap ($E_g$) was determined using Diffuse Reflectance UV-Vis measurements (DR-UV-Vis). Figure 2A shows the spectra for the samples with a nominal composition of Cd of 0 at.%, 25 at.%, and 50 at.%, and the spectrum of $PbI_2$ used as a reagent in the synthesis. For the samples with Cd, two absorption bands are observed in the spectra. The first is at about 540 nm and is assigned to the presence of $PbI_2$. For the sample without $Cd^{2+}$, which is composed of $MAPbI_3$, this absorption band is observed but its intensity is low, which is coherent with the XRD results shown above. The second absorption band observed is at about 830 nm. This is assigned to the presence of perovskite phase in the samples.[12] In turn, a shift of this band towards a higher wavelength was observed when the nominal composition of Cd increased in the samples, that is from 0 at.% to 25 at.% and 50 at.%. This led to a decrease in the optical band gap for the perovskite with $Cd^{2+}$ and $Pb^{2+}$, which suggests that the incorporation of $Cd^{2+}$ into the perovskite structure is obtained up to 50 at.% of Cd.

The optical band gap for the perovskite phases in the samples can be determined from the UV-Vis spectra in diffuse reflectance mode. The optical absorption coefficient ($\alpha/S$) can be calculated by means of reflectance using the Kubelka-Munk formulism,[53]

$$\frac{\alpha}{S} = F(R) = \frac{(1-R)^2}{2R} \qquad (3)$$

where $R$ is the light reflected (%), $\alpha$ is the absorption coefficient and $S$ the scattering coefficient. Moreover, the optical band gap is related to the incident photon energy ($h\nu$) according to the Tauc plot, that is[54, 55]

$$[F(R)h\nu]^p = A\left(h\nu - E_g\right) \qquad (4)$$

where $A$ is a constant depending on the transition probability and $p$ is related to the optical absorption process. Theoretically, $p$ equals ½ or 2 for an indirect or a direct allowed transition, respectively.[19] The optical absorption for this kind of perovskite occurs by direct transition, as reported previously.[28] So, the optical band gap was determined from the extrapolation of the linear part of the Tauc plot with $p = 2$. The values of the optical band gap obtained were 1.57 eV, 1.50 eV and 1.43 eV for the samples with a nominal composition of Cd of 0 at.%, 25 at.% and 50 at.%, respectively. A decrease of around 9% in the band gap value was obtained when $Cd^{2+}$ was incorporated into the perovskite structure in the $Pb^{2+}$ position.

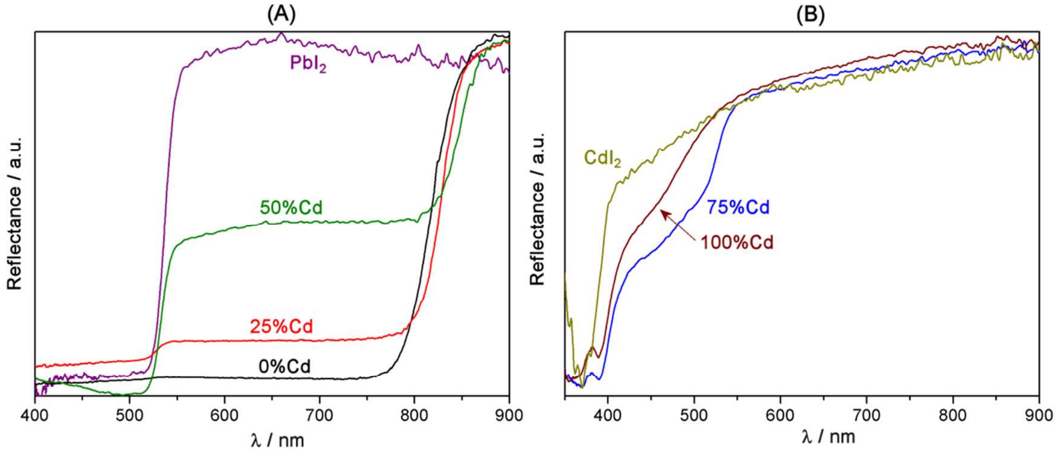

**Figure 2.** UV-Vis spectra, in diffuse reflectance mode, of the samples synthesized.

Figure 2B shows the spectra for the samples with a nominal composition of Cd of 75%, and 100%, and the spectrum of $CdI_2$ used as reagent in the synthesis. For these samples, the presence of the perovskite absorption band is not observed. Moreover, the presence of the typical absorption band for $CdI_2$ at about 390 nm, seen in the DR-UV-Vis spectrum for $CdI_2$ used as reagent, is observed in the samples with a nominal composition of Cd of 75 at.% and 100 at.%. Moreover, for the sample 75 at.% of Cd, it is possible to observe the typical absorption band for $PbI_2$. So, these spectra are further evidence of the non-reaction between $CH_3NH_3I$, $PbI_2$ and $CdI_2$ for higher proportions of Cd, or when $PbI_2$ is not present, for obtaining perovskites structures. Thus, the results seem to indicate that a high proportion of $Cd^{2+}$ in the samples (75 at.% and 100 at.% for the Cd/(Cd+Pb ratio)) impedes the formation of the perovskite structure, the presence of the reactants used for its synthesis being observed. The presence of $CH_3NH_3I$ is not detected with UV-Vis, as its absorption band overlaps the one assigned to the $CdI_2$. The UV-Vis spectrum, in diffuse reflectance mode, for $CH_3NH_3I$ used as a reagent is shown in Figure S1 in the ESI.

## 3.4. XPS

XPS spectra were recorded to study the oxidation and bonding states of the elements in the samples. The samples with a nominal composition of 25 and 75 at.% of Cd were studied. Figure S2 in the ESI shows the general spectra for these samples. Moreover, Figure 3A shows the Pb 4f spectra for these samples. The Pb $4f_{7/2}$ signals appear at the binding energy (BE) of about 139 eV, in good agreement with the values reported previously.[56, 57] Moreover, the spectra show well-separated spin-orbit components, with a separation of about 5 eV in both cases, which is typical for $Pb^{2+}$.

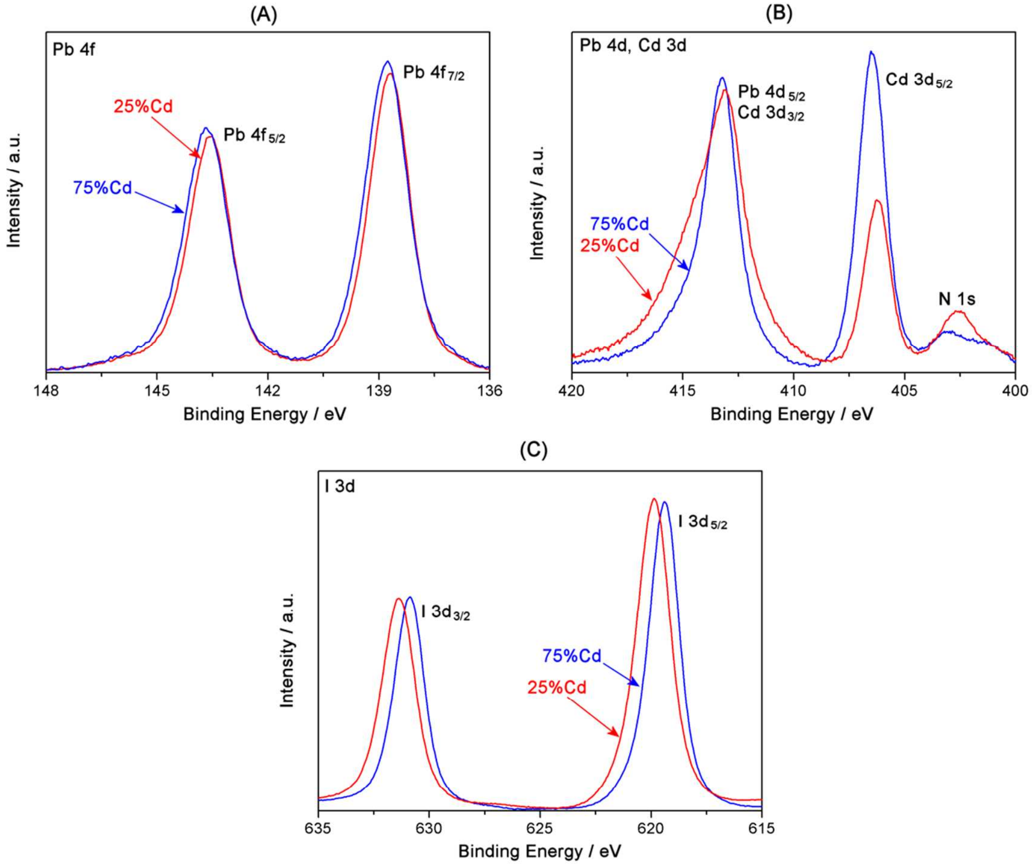

**Figure 3.** XPS spectra for: (A) Pb 4f; (B) Pb 4d and Cd 3d; and (C) I 3d for the samples with a nominal composition of 25 and 75 at.% Cd.

Figure 3B shows the spectrum of the Cd 3d. The signal of the Cd $3d_{3/2}$ completely overlaps that of the Pb $4d_{5/2}$ at approximately 413 eV. This signal is asymmetrical due to the presence of several contributions to it. Furthermore, the signal changes shape depending on the Cd content in the samples. The BE of Cd $3d_{5/2}$ was found at about 406.2 eV, in agreement with the literature for $Cd^{2+}$.[56] The intensity ratio between the signals shown in Figure 3B varies due to the different amounts of Cd in the samples. The signal observed at a BE of about 402.5 eV in Figure 3B is assigned to N 1s.

Figure 3C shows the I $3d_{3/2}$ and I $3d_{5/2}$ spectra for the samples. The spectra show well-separated spin-orbit components, with a separation of about 11.5 eV in both cases, which is in agreement with values reported for $I^-$.[56] Moreover, a shift towards a lower BE is observed in the samples with a higher nominal composition of Cd, which is coherent for compounds of a more ionic nature. So, this typical shift suggests small modifications in the oxidation state of $I^-$ occurred in accordance with the amount of $Cd^{2+}$ in the samples. In fact, the decrease in the optical band gap for the perovskite samples suggests that the presence of Cd slightly modifies the interactions of the ions in the lattice, which leads to changes in the band gap and geometrical distortions in the lattice, as theoretical calculations show.

### 3.5. Structure and local geometry analysis

From a theoretical perspective, an analysis was performed into the effect of increasing the concentration of Cd on the structural and electronic properties of $MAPbI_3$ perovskites. Likewise, a study was performed of the tetragonal structures of $MAPb_{1-x}Cd_xI_3$ with x=0.00, 0.25, 0.50, 0.75 and 1.00.

The local geometry for the most stable configuration of the optimised structures is shown in Figure 4. Our theoretical results show that the incorporation of $Cd^{2+}$ ions caused distortions in the structure. Generally, the inclusion of $Cd^{2+}$ ions produced a

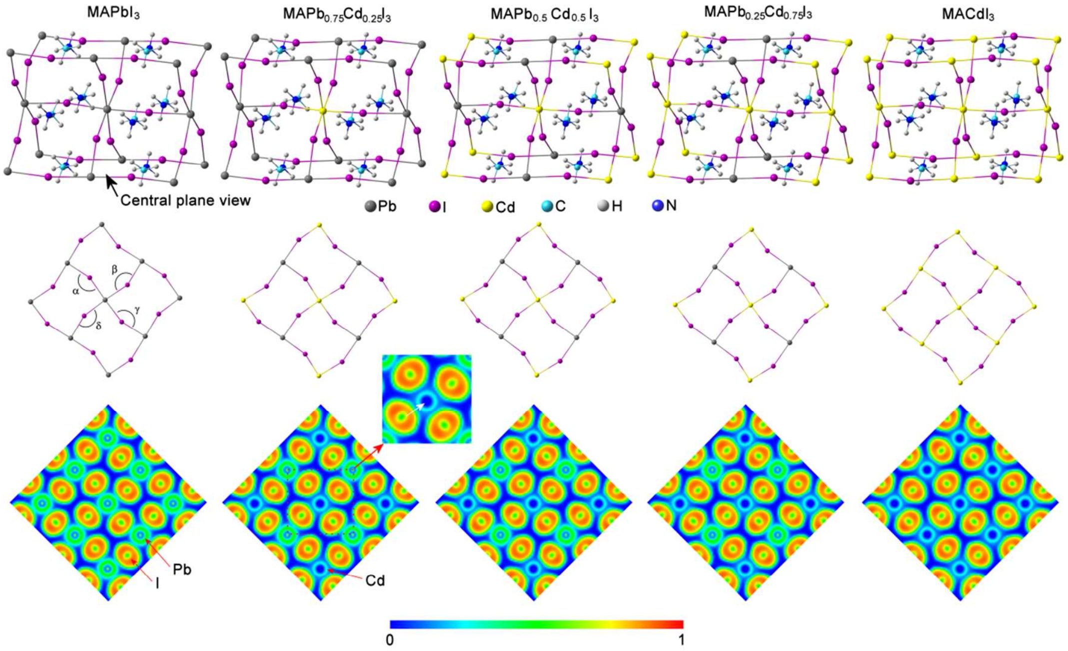

**Figure 4.** The local geometry in 2D and 3D and ELF contour plots for the tetragonal $MAPb_{1-x}Cd_xI_3$ perovskite with x=0.00, 0.25, 0.50, 0.75 and 1.00.

shortening of the Cd-I distances compared with the Pb-I ones. This change is more noticeable for the $MAPb_{0.75}Cd_{0.25}I_3$ and $MAPb_{0.50}Cd_{0.50}I_3$ structures (*c.a.* 3-5% in both) than for the $MAPb_{0.25}Cd_{0.75}I_3$ structures (*c.a.* 1-2%) and $MACdI_3$ (*c.a.* 1%). These modifications to the Cd-I and I-Pb distances are reflected in the changes in the values of the Pb-I-Cd and Cd-I-Cd angles (Figure 4, Table 4). As an example and for clarity, these angles are represented as α, β, γ, and δ in Figure 4. The ESI includes the cut corresponding with the front face of the tetragonal structure (Figure S3) and a table with its angles (Table S2). As Table 4 shows, in general the α, β, γ and δ angles increase in accordance with the concentration of Cd, reaching their highest values in the $MACdI_3$ structure. In turn, the γ and δ angles in the $MACdI_3$ structure are *c.a.* 10 and 5º bigger than the same angles for the $MAPbI_3$ structure. These geometry results lead us to believe that the structural tensions in the theoretical structures $MAPb_{0.25}Cd_{0.75}I_3$ and $MACdI_3$ are greater than in the structures with low concentrations of $Cd^{2+}$ ions.

Therefore, it would seem that a certain concentration of $Pb^{2+}$ ions must be present to stabilise the structure, as shown experimentally and as the results from ELF and NCI indicate, and which will be discussed below.

**Table 4.** Geometrical parameters, identified in Figure 4, of the structures studied.

| Structure | α | β | γ | δ |
|---|---|---|---|---|
| $MAPbI_3$ | 157.11 | 155.03 | 156.52 | 158.35 |
| $MAPb_{0.75}Cd_{0.25}I_3$ | 157.98 | 155.22 | 158.38 | 160.33 |
| $MAPb_{0.50}Cd_{0.50}I_3$ | 158.71 | 155.33 | 160.02 | 161.95 |
| $MAPb_{0.25}Cd_{0.75}I_3$ | 159.03 | 155.30 | 161.19 | 163.19 |
| $MACdI_3$ | 159.85 | 157.02 | 166.40 | 163.48 |

The lower part of Figures 4 and S3 show the ELF plots corresponding to the geometries represented in 2D. Figure 4 shows how the contour plot for Pb is different to that of Cd. It shows that for the experimentally-formed $MAPbI_3$, structure, the outlines of the ELF for I and Pb almost overlap by means of slight electron localization (sky blue colour) that provides more stability to the Pb-I interaction. The introduction of Cd produces directionality in the outlines of the electron localization of the I towards the Cd, which explains the decrease produced in the Cd-I distances. As an example, this directionality is shown as an arrow in the enlarged image of the ELF for the $MAPb_{0.75}Cd_{0.25}I_3$ structure. However, for the $MAPb_{0.75}Cd_{0.25}I_3$, $MAPb_{0.50}Cd_{0.50}I_3$ and $MAPb_{0.25}Cd_{0.75}I_3$ structures, there is a sky blue area between the Pb and I atoms due to the electron localization between them. For the $MACdI_3$ structure, a double directionality can be observed of the I towards each Cd, which explains the variation in the angles stated above (Table 4). This effect is also observed in the ELF image of the $MAPb_{0.25}Cd_{0.75}I_3$ structure in Figure S3 in the ESI. The results of the analysis of the ELF show that a certain proportion of Pb must be present for the perovskite structure to be formed and that the Pb-I interaction provides the structure with a stabilizing effect. At this point, it is interesting to use the NCI index,[18] an analysis tools that complements ELF and is useful for studying weak interactions. This index enables the qualitative identification and characterisation of weak interactions of various strengths as chemically intuitive isosurfaces that reveal both stabilizing (strong and attractive interactions in blue, weak interactions in green) and destabilizing interactions (strong and repulsive interactions in red). Figure 5 shows a comparison of the NCI plots for the I-Pb-I, I-Cd-I-Pb-I and I-Cd-I interactions for the $MAPbI_3$, $MAPb_{0.50}Cd_{0.50}I_3$ and $MACdI_3$ structures, respectively. The ESI includes the NCI plots for the remaining structures (Figure S4) as well as multimedia files (video) with the NCI analysis for all the structures. Comparing Figures 5A and 5B, it is interesting that the experimentally formed structures ($MAPbI_3$ and $MAPb_{0.50}Cd_{0.50}I_3$) show isosurfaces in blue for the Pb-I and Cd-I-Pb interactions. However, for the $MACdI_3$ structure, which was not formed experimentally, the Cd-I isosurface lobes are a green-blue colour, which shows that this interaction is weaker compared with the previous ones. Bearing in mind the tones of the isosurfaces, it is clear that the presence of Pb, particularly above a certain concentration, provides stabilizing characteristics to the Pb-I interaction, which promotes the formation of these perovskite-type structures. In this sense, the $MAPb_{0.25}Cd_{0.75}I_3$ structure that was not formed experimentally provides crucial evidence of this (see Figure S4 and multimedia files in the ESI). Figure S4 shows a majority of Cd-I interactions of a green-blue colour, compared with the uniform blue colour of the Pb-I interaction. This greater strength of the Pb-I interactions means that the structures with a certain amount of Pb are more stable, so they can be formed experimentally. In the case of the $MAPb_{0.25}Cd_{0.75}I_3$ structure, the smaller presence of strong interactions leads us to believe that the structure is less stable, which is coherent with the fact that it is not formed experimentally. Of course, all of the above does not mean that the interactions of other perovskite-type experimental structures will present green-blue interactions, as the formation of these structures is known to present a wide range of exceptions.[49, 50] These results are coherent with the experimental results shown previously.

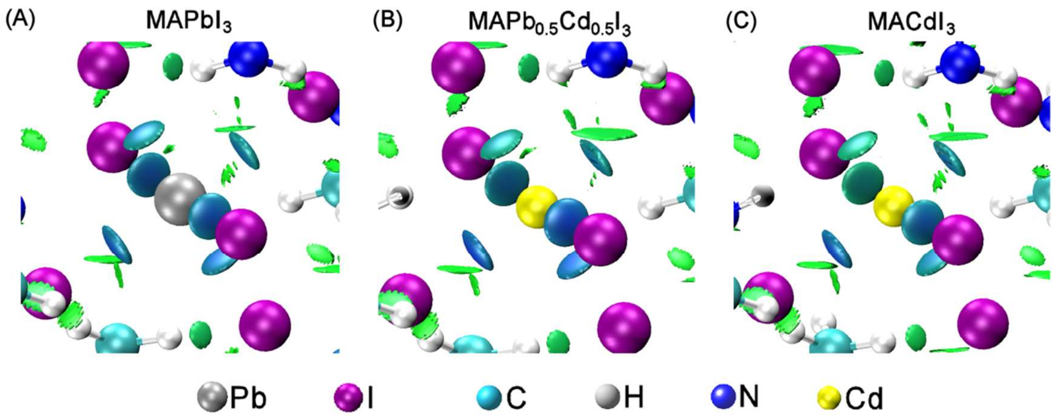

**Figure 5.** NCI plots for tetragonal structures: (A) $MAPbI_3$; (B) $MAPb_{0.5}Cd_{0.5}I_3$; (C) $MACdI_3$.

3.6. DOS and PDOS analysis

To deepen our understanding of the electronic properties that underlie the geometrical effects mentioned above, we will discuss the electronic structure in terms of the density of states (DOS), the projected density of states (PDOS) and the band structure analysis.

The band gaps calculated using the DOS analysis decreased with higher concentrations of Cd (see Figure 6). This smaller band gap is in agreement with the tendency observed experimentally for the perovskite structures formed. Figure 6 compares the DOS with and without SOC. Although, qualitatively, they follow the same trend, the band gap values calculated when the SOC is taken into account are slightly lower than those without SOC.

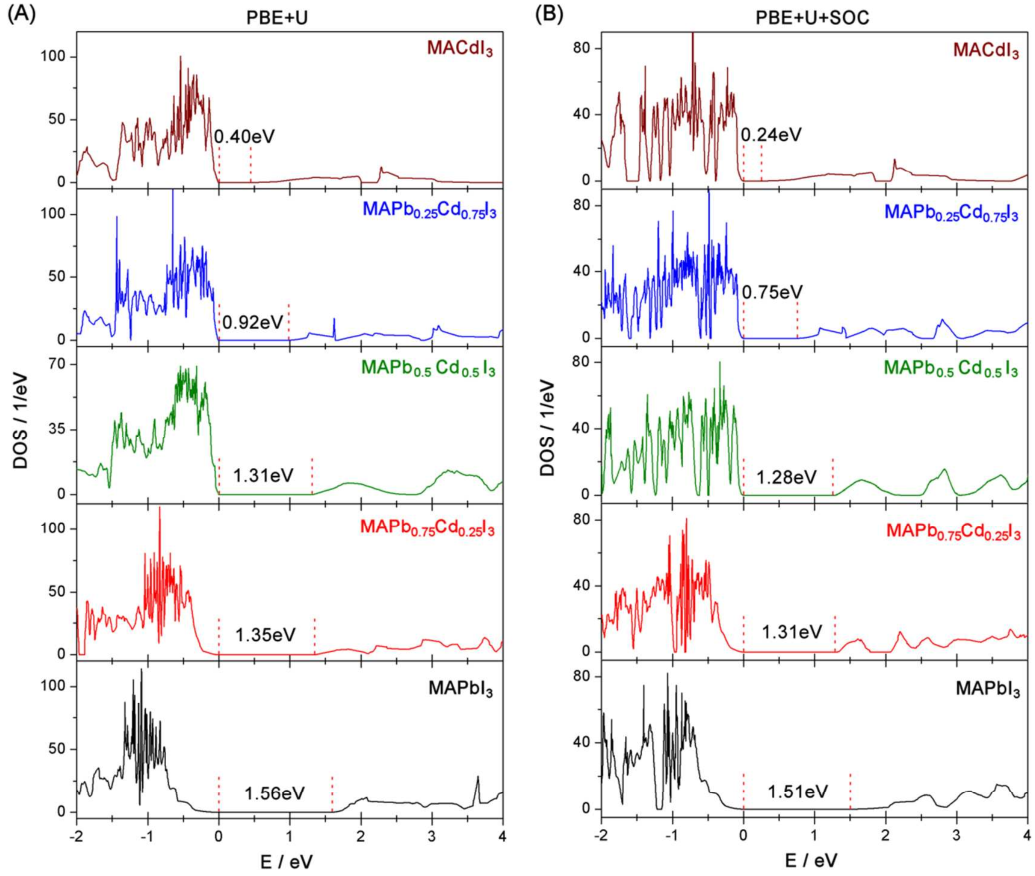

**Figure 6.** Total DOS for tetragonal perovskite structures analysed with and without SOC.

Figure 7 shows the contribution of Pb, Cd, I and MA groups to the valence band (VB) and conduction band (CB) for the $MAPbI_3$, $MAPb_{0.50}Cd_{0.50}I_3$ and $MACdI_3$ structures, which were chosen as being representative for the discussion below. Figure S5 in the ESI includes the same contributions for the $MAPb_{0.75}Cd_{0.25}I_3$ and $MAPb_{0.25}Cd_{0.75}I_3$ structures. Figure S6 shows the PDOS for all structures without SOC. In the figures, the contributions of I atoms and MA groups are represented as total I (s, p and d states of I atoms) and total CHN (s and p states of C and N, and s states of H), respectively. The analysis of the projected density of states (PDOS) of the structures simulated indicates that the VB is mostly composed of I p states, and the CB of the s, p and d states of the $Pb^{2+}$ and $Cd^{2+}$ ions, depending on the structure analysed. For the $MAPbI_3$ structure, the

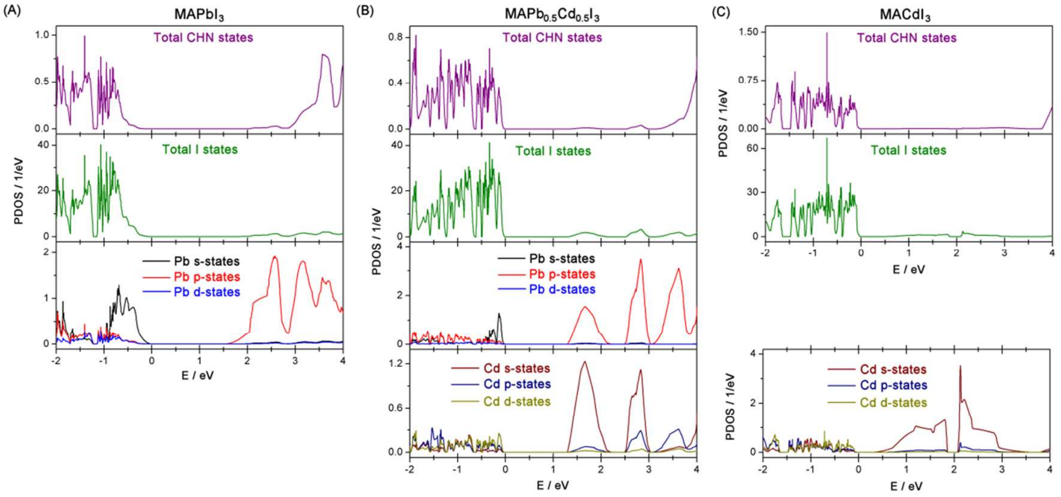

**Figure 7.** Total CHN, total I, Pb and Cd projected states with SOC+U for tetragonal structures: (A) MAPbI$_3$; (B) MAPb$_{0.5}$Cd$_{0.5}$I$_3$; (C) MACdI$_3$.

VB and CB are mostly composed of I p and Pb p states (see Figure 7A) respectively, as reported elsewhere.[12, 30] Likewise, Figure 7A shows that the s and p states of the Pb make the biggest contribution to the edges of the VB and CB, respectively, while the MA groups contribute more internally. In Figure 7B, for the MAPb$_{0.50}$Cd$_{0.50}$I$_3$ structure, as well as the I and CHN states, it is possible to see that the s states of the Pb together with the d states of the Cd make the biggest contribution to the edge of the VB. In particular, the d states that are near the edge of the VB must play an important role in the charge transfer processes. The origin of the CB is dominated by the s states of the Cd followed by the p states of the Pb (Figure 7B). A different situation is observed for the MACdI$_3$ structure, where the I states contribute almost exclusively to the edge of the VB while the s states of the Cd make an extraordinary contribution to the origin of the conduction band (Figure 7C). The analysis of the PDOS shows that the contribution of the s states of the Cd to the origin of the conduction band (CB) plays a fundamental role in the decrease in the band gap (Figure 6). This decrease in the band gap values can be seen more clearly in Figure 8, where the Cd s states in the CB have been superimposed for the $MAPb_{0.75}Cd_{0.25}I_3$, $MAPb_{0.50}Cd_{0.50}I_3$, $MAPb_{0.25}Cd_{0.75}I_3$ and $MACdI_3$ structures. Figure 8 shows the shift to lower gap values of the Cd s states as the concentration of Cd increases.

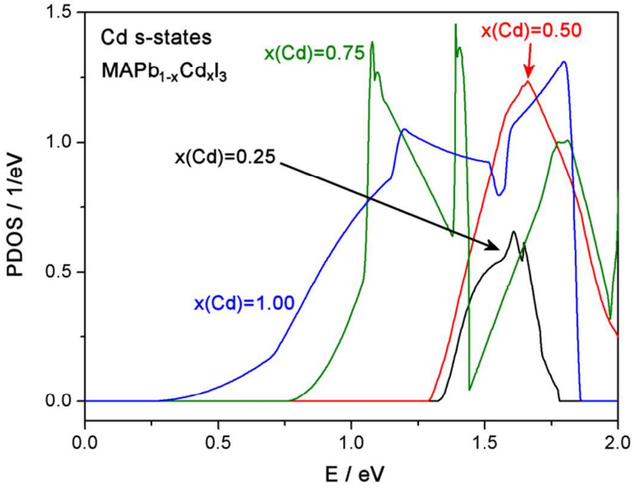

**Figure 8.** Cd projected s-states for tetragonal perovskite structures analysed with SOC+U.

In turn, Figure 9 shows the band structure for the $MAPbI_3$, $MAPb_{0.50}Cd_{0.50}I_3$ and $MACdI_3$ structures. The Brillouin Zone for the tetragonal lattice was chosen as described in the literature.[28] As Figure 9A and 9C show, the transition from VB towards CB for the $MAPbI_3$ and $MACdI_3$ structures is direct and takes place at point Γ. However, the transition for $MAPb_{0.50}Cd_{0.50}I_3$ is indirect (Figure 9B). The valence-band-maximum (VBM) corresponds to point Γ and the conduction-band-minimum (CBM) to point R. For the $MAPbI_3$ structure, a splitting of the bands away from the critical point[36] associated with the loss of inversion symmetry has been reported. This splitting in the presence of SOC is also produced in the $MAPb_{0.50}Cd_{0.50}I_3$ and $MACdI_3$ structures. Nevertheless, strangely, the splitting for both the $MAPb_{0.50}Cd_{0.50}I_3$ and $MACdI_3$ around the critical point R and G, respectively, is less striking than that observed for the $MAPbI_3$ structure (Figure 9D). This result shows the marked effect of lead in this kind of hybrid materials.

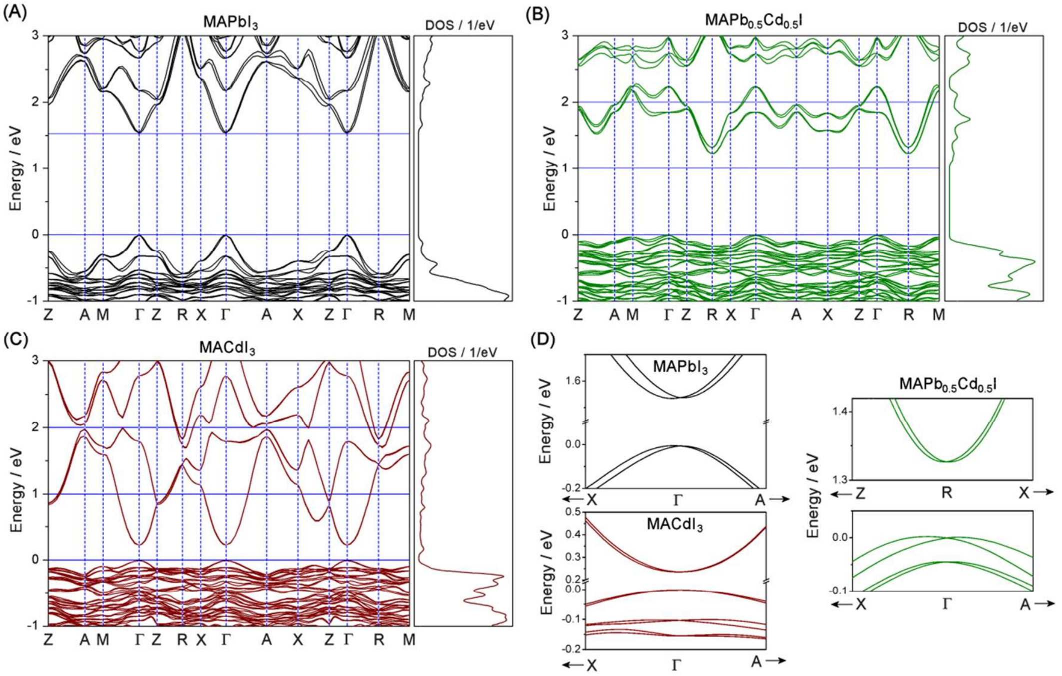

**Figure 9.** Band structure with SOC+U for tetragonal structures: (A) $MAPbI_3$; (B) $MAPb_{0.5}Cd_{0.5}I_3$; and (C) $MACdI_3$. A detail of splitting associated with the loss of inversion symmetry is shown in (D). Γ (0.0,0.0,0.0); M (0.5, 0.5,0.0); Z (0.0,0.0,0.5); X (0.0,0.5,0.0); A (0.5,0.5,0.5); R (0.0,0.5,0.5).

## 4. Conclusions

This paper presents the synthesis of organic-inorganic perovskite $CH_3NH_3Pb_{1-x}Cd_xI_3$. XRD showed the formation of tetragonal perovskite phase for *x* values of up to 0.5, while for values of $x > 0.5$ the perovskite phase was not formed and evidence was found of crystalline phases of the reactants used in the synthesis. The geometrical analysis seems to indicate that the $Cd^{2+}$ ion was small and its incorporation into the octahedral geometry of the perovskite structure was not satisfactory. For this reason, the presence of a large quantity of $Pb^{2+}$ ions was what made possible the stabilization of the tetragonal perovskite structure in the system studied. In addition, DR-UV-Vis spectroscopy showed that the optical band gap value of the perovskite structure decreased when the amount of Cd increased. The optical band gap values decreased by 9% for the $MAPb_{0.5}Cd_{0.5}I_3$ structure with regard to the $MAPbI_3$ structure.

The tendency followed by the band gap values calculated by means of DOS was in agreement with that obtained experimentally. In this sense, the s states of the Cd played a very important role in narrowing the band gap between the valence-band-maximum (VBM) and the conduction-band-minimum (CBM). The band structure analysis shows an indirect transition between VBM and the conduction-band-minimum CBM for $MAPb_{0.75}Cd_{0.25}I_3$, $MAPb_{0.50}Cd_{0.50}I_3$ and $MAPb_{0.25}Cd_{0.75}I_3$ structures.

The ELF and NCI analyses complemented these results and suggested that a certain proportion of $Pb^{2+}$ must be present for the perovskite-type structure to be formed and in this regard the Pb-I interaction provides a stabilizing effect to this kind of hybrid systems, which is in agreement with the experimental results found. Finally, the NCI analysis indicated that the Cd-I interaction was weaker in the structures with a high percentage of Cd than in those with low percentages.

## Acknowledgements

We thank the Junta de Andalucía of Spain under projects P09-FQM-04938, and FEDER funds. Calculations were done through CICA – Centro Informático Científico de Andalucía (Spain).

**Electronic Supplementary Information** (ESI) available: **Table S1.** Results obtained from the elemental analysis performed using CHNS and XRF techniques. **Figure S1.** UV-Vis spectrum for $CH_3NH_3I$ used as a reagent. **Figure S2.** General XPS spectra for the samples with a nominal composition of 25 and 75 at.% Cd. **Figure S3.** The local geometry in 2D and 3D and ELF contour plots for the tetragonal $MAPb_{1-x}Cd_xI_3$ perovskite with x=0.00, 0.25, 0.50, 0.75 and 1.00. **Table S2.** Geometrical parameters, identified in Figure S3. **Figure S4.** NCI plots for tetragonal structures: $MAPb_{0.75}Cd_{0.25}I_3$ and $MAPb_{0.25}Cd_{0.75}I_3$. NCI videos of the structures. **Figure S5.** PDOS for tetragonal structures: $MAPb_{0.75}Cd_{0.25}I_3$ and $MAPb_{0.25}Cd_{0.75}I_3$. See DOI: 10.1039/x0xx00000x

## References

1. G. Murtaza, I. Ahmad, B. Amin, A. Afaq, M. Maqbool, J. Maqssod, I. Khan and M. Zahid, *Opt Mater*, 2011, **33**, 553-557.
2. C. Weeks and M. Franz, *Phys Rev B*, 2010, **82**.
3. P. J. Baker, T. Lancaster, I. Franke, W. Hayes, S. J. Blundell, F. L. Pratt, P. Jain, Z. M. Wang and M. Kurmoo, *Phys Rev B*, 2010, **82**.
4. Y. Y. Li, G. L. Zheng, C. K. Lin and J. Lin, *Cryst Growth Des*, 2008, **8**, 1990-1996.
5. F. Hao, C. C. Stoumpos, R. P. H. Chang and M. G. Kanatzidis, *J Am Chem Soc*, 2014, **136**, 8094-8099.
6. M. M. Lee, J. Teuscher, T. Miyasaka, T. N. Murakami and H. J. Snaith, *Science*, 2012, **338**, 643-647.
7. N. G. Park, *Mater Today*, 2015, **18**, 65-72.
8. C. Bellitto, E. M. Bauer and G. Righini, *Coordination Chemistry Reviews*, 2015, **289-290**, 123-136.
9. M. Graetzel, R. A. J. Janssen, D. B. Mitzi and E. H. Sargent, *Nature*, 2012, **488**, 304-312.
10. Y. Ogomi, A. Morita, S. Tsukamoto, T. Saitho, N. Fujikawa, Q. Shen, T. Toyoda, K. Yoshino, S. S. Pandey, T. L. Ma and S. Hayase, *J Phys Chem Lett*, 2014, **5**, 1004-1011.
11. P. Umari, E. Mosconi and F. De Angelis, *Sci Rep-Uk*, 2014, **4**.
12. J. Navas, A. Sanchez-Coronilla, J. J. Gallardo, N. C. Hernandez, J. C. Pinero, R. Alcantara, C. Fernandez-Lorenzo, D. M. De los Santos, T. Aguilar and J. Martin-Calleja, *Nanoscale*, 2015, **7**, 6216-6229.
13. A. D. Becke and K. E. Edgecombe, *J Chem Phys*, 1990, **92**, 5397-5403.
14. B. Silvi and A. Savin, *Nature*, 1994, **371**, 683-686.
15. B. Silvi and C. Gatti, *J Phys Chem A*, 2000, **104**, 947-953.
16. A. Savin, A. D. Becke, J. Flad, R. Nesper, H. Preuss and H. G. Vonschnering, *Angew Chem Int Edit*, 1991, **30**, 409-412.
17. A. Savin, O. Jepsen, J. Flad, O. K. Andersen, H. Preuss and H. G. Vonschnering, *Angew Chem Int Edit*, 1992, **31**, 187-188.
18. E. R. Johnson, S. Keinan, P. Mori-Sanchez, J. Contreras-Garcia, A. J. Cohen and W. T. Yang, *J Am Chem Soc*, 2010, **132**, 6498-6506.
19. H. S. Kim, C. R. Lee, J. H. Im, K. B. Lee, T. Moehl, A. Marchioro, S. J. Moon, R. Humphry-Baker, J. H. Yum, J. E. Moser, M. Gratzel and N. G. Park, *Sci Rep-Uk*, 2012, **2**.
20. S. R. Jang, K. Zhu, M. J. Ko, K. Kim, C. Kim, N. G. Park and A. J. Frank, *Acs Nano*, 2011, **5**, 8267-8274.
21. G. Kresse and J. Hafner, *Phys Rev B*, 1993, **47**, 558-561.
22. G. Kresse and J. Hafner, *Phys Rev B*, 1994, **49**, 14251-14269.
23. G. Kresse and J. Furthmuller, *Comp Mater Sci*, 1996, **6**, 15-50.
24. G. Kresse and J. Furthmuller, *Phys Rev B*, 1996, **54**, 11169-11186.
25. P. E. Blochl, *Phys Rev B*, 1994, **50**, 17953-17979.
26. G. Kresse and D. Joubert, *Phys Rev B*, 1999, **59**, 1758-1775.
27. J. P. Perdew, K. Burke and M. Ernzerhof, *Physical Review Letters*, 1996, **77**, 3865-3868.
28. E. Mosconi, A. Amat, M. K. Nazeeruddin, M. Gratzel and F. De Angelis, *J Phys Chem C*, 2013, **117**, 13902-13913.

29. J. Even, L. Pedesseau, M. A. Dupertuis, J. M. Jancu and C. Katan, *Phys Rev B*, 2012, **86**.
30. T. Baikie, Y. N. Fang, J. M. Kadro, M. Schreyer, F. X. Wei, S. G. Mhaisalkar, M. Graetzel and T. J. White, *J Mater Chem A*, 2013, **1**, 5628-5641.
31. A. Poglitsch and D. Weber, *J Chem Phys*, 1987, **87**, 6373-6378.
32. P. E. Blochl, O. Jepsen and O. K. Andersen, *Phys Rev B*, 1994, **49**, 16223-16233.
33. S. L. Dudarev, G. A. Botton, S. Y. Savrasov, C. J. Humphreys and A. P. Sutton, *Phys Rev B*, 1998, **57**, 1505-1509.
34. E. Menendez-Proupin, A. Amezaga and N. C. Hernandez, *Physica B*, 2014, **452**, 119-123.
35. J. Even, L. Pedesseau, J. M. Jancu and C. Katan, *J Phys Chem Lett*, 2013, **4**, 2999-3005.
36. J. Even, L. Pedesseau, J. M. Jancu and C. Katan, *Phys Status Solidi-R*, 2014, **8**, 31-35.
37. L. Hedin, *Phys Rev*, 1965, **139**, A796-+.
38. M. S. Hybertsen and S. G. Louie, *Phys Rev B*, 1986, **34**, 5390-5413.
39. H. Nakamura, M. Machida and M. Kato, *Progress in Nuclear Science and Technology*, 2011, **2**, 16-19.
40. T. B. Terriberry, D. F. Cox and D. A. Bowman, *Comput Chem*, 2002, **26**, 313-319.
41. www.chemcraftprog.com).
42. A. Otero-de-la-Roza, M. A. Blanco, A. M. Pendas and V. Luana, *Comput Phys Commun*, 2009, **180**, 157-166.
43. A. Otero-de-la-Roza, E. R. Johnson and V. Luana, *Comput Phys Commun*, 2014, **185**, 1007-1018.
44. W. Humphrey, A. Dalke and K. Schulten, *J Mol Graph Model*, 1996, **14**, 33-38.
45. J. Burschka, N. Pellet, S. J. Moon, R. Humphry-Baker, P. Gao, M. K. Nazeeruddin and M. Gratzel, *Nature*, 2013, **499**, 316-+.
46. A. Kojima, K. Teshima, Y. Shirai and T. Miyasaka, *J Am Chem Soc*, 2009, **131**, 6050-+.
47. J. H. Noh, S. H. Im, J. H. Heo, T. N. Mandal and S. I. Seok, *Nano Lett*, 2013, **13**, 1764-1769.
48. V. M. Goldschmidt, *Ber Dtsch Chem Ges*, 1927, **60**, 1263-1296.
49. C. H. Li, X. G. Lu, W. Z. Ding, L. M. Feng, Y. H. Gao and Z. G. Guo, *Acta Crystallogr B*, 2008, **64**, 702-707.
50. L. M. Feng, L. Q. Jiang, M. Zhu, H. B. Liu, X. Zhou and C. H. Li, *J Phys Chem Solids*, 2008, **69**, 967-974.
51. R. D. Shannon, *Acta Crystallogr A*, 1976, **32**, 751-767.
52. D. R. Lide, *CRC Handbook of Chemistry and Physics. 90th Edition*, CRC Press, Boca Raton, Florida, USA, 2009.
53. L. F. Gate, *Appl Optics*, 1974, **13**, 236-238.
54. N. Serpone, D. Lawless and R. Khairutdinov, *J Phys Chem-Us*, 1995, **99**, 16646-16654.
55. J. Navas, A. Sanchez-Coronilla, T. Aguilar, N. C. Hernandez, D. M. de los Santos, J. Sanchez-Marquez, D. Zorrilla, C. Fernandez-Lorenzo, R. Alcantara and J. Martin-Calleja, *Phys Chem Chem Phys*, 2014, **16**, 3835-3845.
56. A. K.-V. A. V. G. Naumkin, S. W.; C. J. Powell, *in NIST Standard Reference Database 20, Version 4.1, Gaithersburg*, 2012.

57. Z. Zheng, S. M. Wang, D. P. Li, A. R. Liu, B. J. Huang, H. X. Zhao and L. Z. Zhang, *J Cryst Growth*, 2007, **308**, 398-405.